A Power-Efficient Multichannel Neural Stimulator Using High-Frequency Pulsed Excitation From an Unfiltered Dynamic Supply

Marijn N. van Dongen, *Member, IEEE*, and Wouter A. Serdijn, *Fellow, IEEE*

***Abstract*—This paper presents a neural stimulator system that employs a fundamentally different way of stimulating neural tissue compared to classical constant current stimulation. A stimulation pulse is composed of a sequence of current pulses injected at a frequency of 1 MHz for which the duty cycle is used to control the stimulation intensity. The system features 8 independent channels that connect to any of the 16 electrodes at the output. A sophisticated control system allows for individual control of each channel's stimulation and timing parameters. This flexibility makes the system suitable for complex electrode configurations and current steering applications. Simultaneous multichannel stimulation is implemented using a high frequency alternating technique, which reduces the amount of electrode switches by a factor 8. The system has the advantage of requiring a single inductor as its only external component. Furthermore it offers a high power efficiency, which is nearly independent on both the voltage over the load as well as on the number of simultaneously operated channels. Measurements confirm this: in multichannel mode the power efficiency can be increased for specific cases to 40% compared to 20% that is achieved by state-of-the-art classical constant current stimulators with adaptive power supply.**

***Index Terms*—Current steering, dynamic power supply, HVCMOS, implantable medical devices, low power, multichannel, neural stimulation.**

I. Introduction

IMPLANTABLE neural stimulators impose strict requirements on the power consumption, safety and size of the system. The number of external components should be kept to a minimum to limit the size and increase the device safety, while the power efficiency should be maximized in order to limit the battery size.

Furthermore there is a trend towards an increasing number of stimulation channels. Some applications, such as cochlear implants [1], vestibular implants [2] or retinal implants [3]–[5], need a high number of channels to accommodate a large amount of stimulation sites. Other applications, such as Deep Brain Stimulation (DBS) [6] or Peripheral Nerve Stimulation (PNS) [7] use multiple channels to implement current steering [8], [9] to achieve more localized neuronal recruitment with fewer side effects.

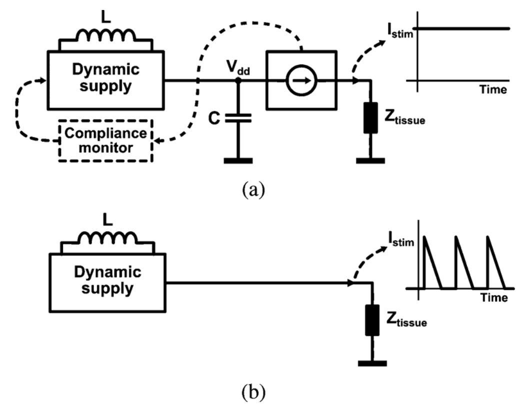

Fig. 1. High level system architectures of (a) a typical (constant) current based stimulator system with adaptive supply and (b) the high-frequency dynamic stimulator proposed in this work.

Current source based stimulation is usually preferred in order to accurately control the amount of charge during a stimulation cycle. A high-level system architecture of a typical current-based stimulator is shown in Fig. 1(a): a power efficient switched voltage converter, here referred to as a dynamic supply, is used to control V_{dd} to supply the current source that generates the stimulation current $I_{\rm stim}$ [10]–[12]. As can be seen this system uses at least two external components (the inductor L and the output capacitor C). Also, as will be shown, the power efficiency degrades when the system is operated in multichannel mode.

In this paper an implementation is discussed that uses the dynamic power supply to stimulate the tissue directly, as shown in Fig. 1(b). The output capacitor is omitted and hence only one external component is required. The exclusion of this capacitor leads to a fundamentally different stimulation principle: L is repeatedly discharged through the load. The stimulation waveform through the load consists of a train of high frequency current pulses, each of which contains a well defined amount of charge.

The proposed system is particularly suitable to operate in multichannel mode. The inductor can be discharged in an alternated fashion through different electrodes with tailored stimulation intensities, making simultaneous and independent stimulation possible over multiple electrodes, without the need for

Manuscript received July 03, 2014; revised September 26, 2014; accepted October 13, 2014. This paper was recommended by Associate Editor M. Stanacevic.

The authors are with Section Bio-electronics, Department of Electrical Engineering, Mathematics and Computer Science, Delft University of Technology, 2628 CD Delft, The Netherlands (e-mail: marijn.v.dongen@ieee.org; w.a.serdijn@tudelft.nl).

Color versions of one or more of the figures in this paper are available online at http://ieeexplore.ieee.org.

Digital Object Identifier 10.1109/TBCAS.2014.2363736

This article has been accepted for inclusion in a future issue of this journal. Content is final as presented, with the exception of pagination.

additional external components. The advantage of the proposed system is that the power efficiency is almost not degraded when it is operated in multichannel mode, as opposed to state of the art current based stimulators.

The paper is organized as follows. In Section II the power efficiency of classical adaptive supply constant current stimulation is analyzed and it is shown how high frequency dynamic stimulation can improve the efficiency. In Section III the system design is discussed, emphasizing the digital control that enables the independent multichannel operation. Section IV subsequently discusses the circuit design of some of the system blocks in detail. Finally in Section V the measurement results of a prototype IC realization are presented, comparing the power efficiency of the proposed system with state of the art current source based systems.

II. High Frequency Dynamic Stimulation

A. Power Efficiency of Current-Source Based Stimulators

The power efficiency of current source based stimulators is in general limited due to the voltage drop over the current driver. A popular way to increase the power efficiency is to adapt the power supply to the load voltage using a compliance monitor [3], [13]. A generic biphasic constant current stimulator setup is depicted in Fig. 2(a) with the load being modeled as a resistance R_{load} and capacitance C_{load} [14]. During stimulation there is a constant voltage drop $V_R = I_{\text{stim}}R_{\text{load}}$ over R_{load}, while the capacitor is charging towards $V_C = I_{\text{stim}}t_{\text{stim}}/C_{\text{load}}$.

The efficiency of an adaptive supply system depends on the ratio $\alpha = V_R/V_C$. Referring to Fig. 2(b), the energy dissipated in the load is $E_{\text{load}} = I_{\text{stim}}V_R t_{\text{stim}} + 0.5V_C I_{\text{stim}} t_{\text{stim}}$. Assuming the supply will adapt to $V_{\text{adapt}} = V_R + V_C + V_{\text{compl}}$ in which V_{compl} is the minimum required compliance voltage for the current driver, the energy delivered by the source is $E_{\text{supply}} = \eta_{\text{sup}}^{-1} I_{\text{stim}} V_{\text{adapt}} t_{\text{stim}}$, in which η_{sup} is the efficiency of the adaptive supply generator. The power efficiency η_{adapt} is now found to be

$$\eta_{\text{adapt}} = \frac{E_{\text{load}}}{E_{\text{supply}}} = \frac{\eta_{\text{sup}} V_C(0.5+\alpha)}{V_C(1+\alpha)+V_{\text{compl}}}. \tag{1}$$

The theoretical maximum efficiency is found with an ideal adaptive supply generator $\eta_{\text{sup}} = 1$ and a current source with $V_{\text{compl}} = 0$

$$\eta_{\text{adapt,ideal}} = \frac{0.5+\alpha}{1+\alpha}. \tag{2}$$

This equation is plotted in Fig. 2(c). Realistic values for η_{adapt} will be lower due to practical values of V_{compl} and η_{sup}. As an example a system is considered with $V_{\text{compl}} = 300$ mV [3] and $\eta_{\text{sup}} = 80\%$ [13], which is connected to a load of $R_{\text{load}} = 500\ \Omega$, $C_{\text{load}} = 1\ \mu$ F and $t_{\text{stim}} = 200\ \mu$A ($\alpha = 1$). The efficiency as a function of I_{stim} is depicted in Fig. 2(d) by the black line (open markers). As can be seen the performance degrades as compared to the theoretical maximum, especially for low stimulation intensities. In the same Figure the efficiency can be compared with a load consisting of $R_{\text{load}} = 500\ \Omega$, $C_{\text{load}} = 10\ \mu$F ($\alpha = 2.5$, red lines, filled markers) and with a classical non adaptive supply system with $V_{dd} = 10$ V (dashed lines).

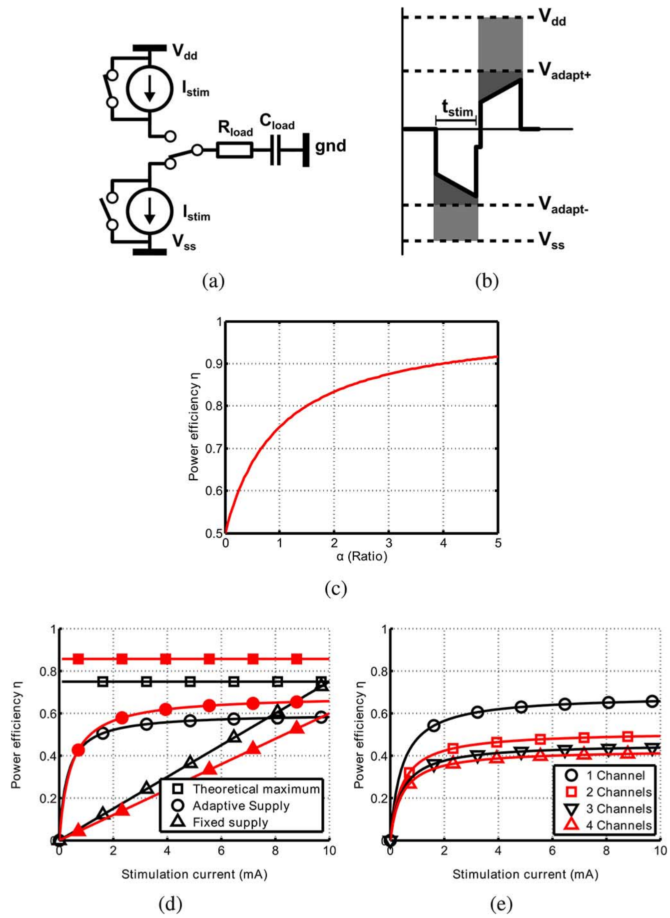

Fig. 2. Power efficiency analysis of a constant current source stimulator with adaptive power supply. In (a), a generic biphasic stimulator is depicted. In (b), the losses due to an adaptive supply stimulator (dark grey) and a fixed supply stimulator (light grey) are visualized. In (c), the theoretical maximum power efficiency is depicted as a function of $\alpha = V_R/V_C$. In (d) and (e), the power efficiency is depicted for a more realistic system. In (d), the black lines (open markers) correspond to a load of $R_{\text{load}} = 500\ \Omega$, $C_{\text{load}} = 1\ \mu$F with $t_{\text{stim}} = 200\ \mu$A ($\alpha = 1$), while the red lines (filled markers) correspond to $R_{\text{load}} = 500\ \Omega$, $C_{\text{load}} = 10\ \mu$F ($\alpha = 2.5$). It is seen in (e) that the efficiency drops dramatically when the system is operated with multiple channels.

The efficiency is even more degraded when the system is operated with multiple channels. Since there is only one supply voltage, this voltage needs to adapt to the channel with the highest $V_R + V_C$. This means that when other channels have a lower $V_R + V_C$, the efficiency is reduced. Such a reduction can be due to two factors. The first factor is impedance variation [15]: clinical values of the impedance spread of electrode contacts within individual DBS patients report standard deviations as high as 500 Ω (mean 1200 Ω) [16]. The second factor is variation in the stimulation intensity, which is common in current steering applications.

As an example the effect of impedance variation on the efficiency in multichannel operation is considered. Multiple loads are stimulated simultaneously with $t_{\text{stim}} = 200\ \mu$A. Channel 1 has $R_{\text{load},1} = 500\ \Omega$ and $C_{dl,1} = 10\ \mu$F, while Channel 2 has $R_{\text{load},2} = 200\ \Omega$ and $C_{dl,2} = 10\ \mu$F. As can be seen

This article has been accepted for inclusion in a future issue of this journal. Content is final as presented, with the exception of pagination.

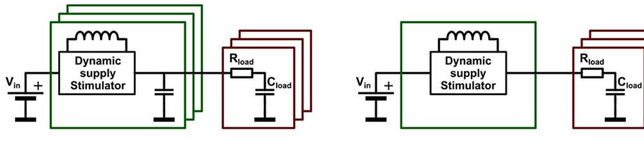

Fig. 3. System setup of dynamic power supply based stimulators. In (a), the system architecture is depicted of [17], while in (b) the proposed architecture is shown. Removal of the output capacitor C_{out} and using only a single dynamic supply allows for efficient multichannel stimulation.

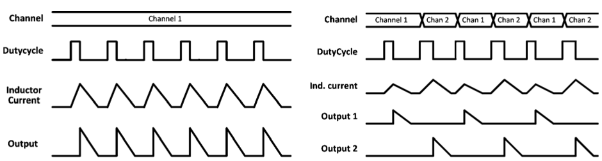

Fig. 4. Sketch of signal waveforms illustrating the working principle of the proposed high frequency stimulator system. In (a), single channel operation is depicted, while in (b) simultaneous dual channel operation is shown in which the stimulus pulses are sent to the load in an alternating fashion.

in Fig. 2(e), the power efficiency for this dual channel operation mode drops from 65% down to 50%, due to the reduced efficiency for Channel 2. Including even more channels with $R_{\mathrm{load},n} = 200\ \Omega$ will decrease the efficiency further to about 40% for 4 simultaneous channels. A similar effect can be found for variations in stimulation current.

B. High Frequency Dynamic Stimulation

A system that is much less sensitive to α was introduced in [17] by using a dynamic supply to drive the load directly, as shown in Fig. 3(a). The output voltage of the dynamic power supply is connected directly to the load, which means that the power efficiency is not dependent on α, but instead on the efficiency of the switched supply.

The system uses at least two external components: the inductor L for the dynamic power supply and a capacitor C_{out} to filter the switched output signal. This system does not scale well if multiple channels need to be controlled independently and simultaneously. Due to the filtering properties of C_{out} the voltage cannot be controlled for multiple channels individually. Furthermore, the stimulation is voltage steered, which means that charge is not controlled directly.

As was outlined in [18], it is proposed to remove C_{out} from the system as shown in Fig. 3(b). A duty cycled signal is used to charge and subsequently discharge the inductor through the load as sketched in Fig. 4(a). In [19] it was shown that this high frequency pulsating stimulation pattern is able to induce effective neuronal recruitment. In short, the electric field in the tissue will have the same pulsating transient behavior as the stimulation pulse. Calculating the response of an axon using a cable model similar as to what is described in [20], it is seen that the pulsating excitation is integrated on the axon membrane surface due to its capacitive properties. The membrane voltage will therefore increase with a 'staircase' shape, eventually leading to recruitment of the axon. *In vitro* measurements have confirmed that indeed a pulsating high frequency stimulation pulse will lead to neuronal recruitment.

In Fig. 3(b) it is illustrated that the proposed system is able to operate in multichannel mode without the need to duplicate the dynamic power supply or the inductor. The operating principle is shown in Fig. 4(b) for two channels. The high frequency pulses are delivered in an alternating fashion to both channels. Also note in Fig. 4(b) that it is possible to stimulate the channels independently with different amplitudes by adjusting the duty cycle for each channel individually, provided the dynamic supply operates in discontinuous mode.

Note that neuronal recruitment depends on the amount of charge injected (as described by the strength-duration curve [21]). This means that despite the fact that the average stimulation current is halved when two channels are operated simultaneously, the amount of charge delivered to the load remains the same as compared to single channel operation.

The power efficiency of the proposed dynamic power supply stimulator ideally does neither depend on α nor on the number of independent channels that are activated simultaneously. Instead it depends on the power efficiency of the dynamic stimulator. In the next section the system design of a high frequency dynamic stimulator is discussed.

III. System Design

A. High Frequency Dynamic Stimulator Requirements

The input of the system is assumed to be a Li-ion battery that is typically used in implantable systems, for which the nominal voltage is around $V_{\mathrm{in}} = 3.5$ V. The system is designed to connect to electrode leads that are used for deep brain and peripheral nerve stimulation. Platinum electrodes manufactured by St. Jude Medical are used that are ring shaped, have an area of approximately 14 mm^2 and for which it was assumed that 100 $\Omega < R_{\mathrm{load}} < 1$ k Ω. The choice for these electrodes is not fundamental: the system can be designed to operate with other types of electrodes as well.

Stimulation amplitudes for these type of electrodes in commercial stimulators are reported up to 10 mA [22], [23]. This means that $V_{\mathrm{out}} = I_{\mathrm{stim}} R_{\mathrm{load}}$ requires both up- and down-conversion with respect to V_{in} over the full range of R_{load}, which means that a buck-boost topology is needed for the dynamic stimulator. To avoid negative output voltages which complicate substrate biasing, it was chosen to use a forward buck-boost topology, which is shown as part of the total system in Fig. 5.

The switching frequency of the dynamic power supply determines the resolution for the pulse width. When N channels are active, the pulse width of each channel can be controlled in step sizes of N/f_{sw} seconds with f_{sw} being the switching frequency. It was chosen to have $f_{\mathrm{sw}} = 1$ MHz such that the maximum step size is 8 μs when all 8 channels are active.

B. General System Architecture

The system design of the stimulator is depicted in Fig. 5. The forward buck-boost converter connects to 2×16 switches that make it possible for the user to select for each stimulation channel one electrode to be the anode and one to be the cathode. The digital control block generates all the necessary control signals to make the stimulator work. It implements 8 channels that have independent stimulation parameters, such as amplitude,

This article has been accepted for inclusion in a future issue of this journal. Content is final as presented, with the exception of pagination.

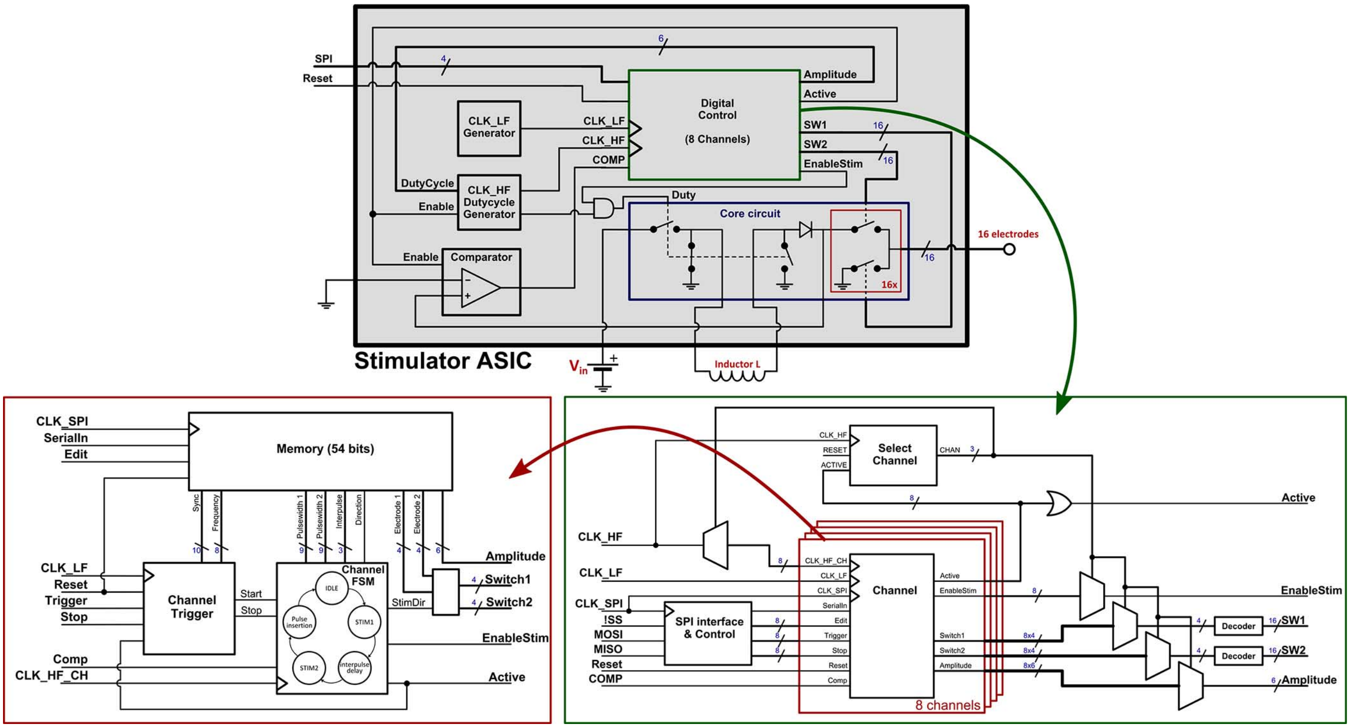

Fig. 5. System design overview. The core of the circuit is formed by a forward buck-boost dynamic supply that directly connects to the 16 electrodes at the output. A digital module, running on two clocks, controls the system and for which a detailed overview is given in the green box. Here the *Select_Channel* block selects out of the 8 channels the active ones and routes the input and output signals accordingly. The red box shows the functionality of a single stimulation channel.

pulsewidth, frequency and the electrodes that are used. Each channel can be configured and controlled individually via an SPI interface.

The control block uses two clocks. The low frequency clock signal CLK_LF with $f_{clk\_lf} = 1$ kHz is always active and is used to trigger stimulation patterns. The high frequency clock *CLK_HF* with $f_{clk\_hf} = f_{sw} = 1$ MHz is used to control the core circuit and is only active when one or more stimulation channels are active. The signal *DUTY* is a duty cycled version of *CLK_HF* that controls the core circuit. The duty cycle is set by the 6 bit *AMPLITUDE* signal.

The comparator is used for charge-cancellation purposes. After a stimulation cycle is finished, the remaining voltage over the electrodes is measured and using pulse insertion [24] the charge is removed from the interface. A single comparator is enough even when the system is operating in multichannel mode, because the remaining voltages are measured one by one for all the active channels, using the same alternating principle as during stimulation [Fig. 4(b)]. Pulse insertion is easy to incorporate in the system, since the stimulation waveform is pulse shaped already.

A biphasic stimulation pulse is generated by reversing the signals $SW1$ and $SW2$ after the first stimulation phase such that the direction of the current through the electrodes is also reversed (H-bridge configuration [11]). Note that multiple channels can share the same electrodes, making the system suitable for many electrode configurations such as mono-, bi- or tripolar as well as more complicated schemes required for field steering techniques. Note that the H-bridge configuration allows reversal of the current (biphasic operation) irrespective of the chosen electrode configuration.

If the same level of flexibility (any channel can connect to any electrode) is to be implemented in a classical current source based stimulator, it would require $8 \times 16 \times 2 = 172$ switches between the 8 current sources and the 16 electrodes. This system architecture therefore reduces the number of required switches by a factor 8 (i.e., by the number of channels).

C. Digital Control Design

In the bottom left corner of Fig. 5 a simplified structure of the block responsible for controlling one stimulation channel is depicted. In the memory 54 bits are used to store the stimulation settings. The memory is loaded via a serial interface when the *EDIT* pin is enabled.

The *Channel_FSM* is a Finite State Machine (FSM) running on *CLK_HF*, where the basic functionality of a stimulation pulse is implemented as discussed in the previous section. After a trigger pulse is received, the FSM loops through the stages of a biphasic stimulation scheme where the pulse durations and inter-pulse delays are obtained by counting a number of *CLK_HF* periods equal to the value from the memory. Afterwards the charge balancing is implemented using pulse insertion. The output signal *ACTIVE* is enabled when the FSM is not in the *IDLE* state, indicating that the channel is operating in a stimulation cycle. The *EnableStim* signal is used to enable the *DUTY* signal during the stimulation and charge cancellation phases.

After receiving a trigger or stop command, the *Channel_Trigger* block is able to start or stop a stimulation cycle in the *Channel_FSM* block in two different ways. When

This article has been accepted for inclusion in a future issue of this journal. Content is final as presented, with the exception of pagination.

TABLE I
COMMANDS USED OVER THE SPI INTERFACE TO PROGRAM THE SYSTEM

Command	Code
Edit Channel	001
Trigger Single Channel	010
Stop Single Channel	011
Global Trigger	100
Global Stop	101

the frequency stored in the memory equals zero, the channel operates in ‘single shot’ mode: whenever it is triggered by an SPI command, a single stimulation sequence is generated. When the frequency is not zero, the channel operates in tonic mode: using *CLK_LF* a stimulation cycle is triggered periodically by counting a number of periods as specified by the value of Frequency. Furthermore it is possible to align multiple channels by setting the *SYNC* value in the memory: upon triggering stimulation is delayed by a number of *CLK_LF* periods equal to the value in *SYNC*. In this way it is possible to accurately trigger multiple channels sequentially with only a single command.

In the green block in Fig. 5 a simplified overview is given of the complete digital control system of the stimulator. At the core are the 8 channels. The *Select_channel* block is an FSM that keeps track of which Channels are currently active. Using (de)multiplexers the inputs and outputs are routed to and from the active channel. If multiple channels are active at the same time, the *Select_channel* block alternates between the active channels.

The *SPI interface & control* block forms the interface with the outside world. The system can be configured with the commands shown in Table I. The Edit Channel command is followed by a 3 bit word to select the channel and subsequently a 42 bit word is sent that contains the data to be stored in the memory of the channel (some of the Least Significant Bits in the 54 bits channel memory have default values). The Trigger and Stop Single Channel commands are also followed by a three bit code that selects the channel to be triggered or stopped. The global trigger and stop command are not followed by more bits.

IV. CIRCUIT DESIGN

A. Dynamic Stimulator

The forward buck-boost topology from Fig. 5 was implemented as shown in Fig. 6. Transistors M_1, M_2 and M_3 form the dynamic supply switches, and M_4 and M_5 are the switches connecting the electrodes. Schottky diode D_1 is used to avoid oscillations in the load, while diode D_2 and switch M_6 are used to avoid oscillations in the inductor. All the gates of the transistors are driven with drivers that include level converters with appropriate voltages.

1) Choice of L: By using a first order Taylor approximation for the charging current of the inductor during the δT interval (δ being the duty cycle and $T = 1/f_{\rm sw}$), the peak current in the inductor is $I_{\rm peak} = V_{\rm in}\delta T/L$ and the energy in the inductor

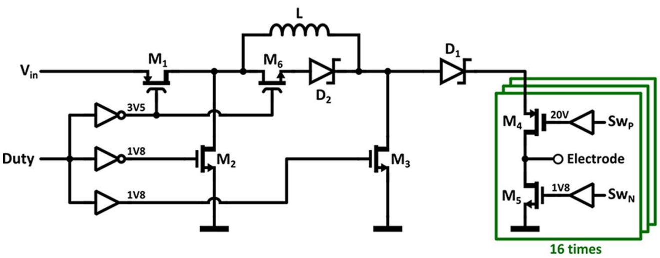

Fig. 6. Circuit implementation of the forward buck-boost dynamic supply.

will be $E_L = 0.5V_{\rm in}^2\delta^2T^2/L$. In the ideal case all this energy is transferred to the load, leading to an average current $I_{\rm avg} = \sqrt{E_L/(R_{\rm load}T)}$. By combining these equations, an expression for the ratio $H = I_{\rm avg}/I_{\rm peak}$ is found

$$H = \frac{I_{\rm avg}}{I_{\rm peak}} = \sqrt{\frac{L}{2TR}} \rightarrow L = 2RT\frac{I_{\rm avg}^2}{I_{\rm peak}^2}. \tag{3}$$

This ratio should not become too small in order to prevent high values of $I_{\rm peak}$. Therefore, for a given minimum H, the minimum value of L is determined.

The maximum value of the inductor is determined by the fact that the system is required to operate in discontinuous mode. For a given maximum duty cycle $\delta_{\rm max} = 0.5$, the inductor needs to be discharged within the time frame $1 - \delta_{\rm max}$. During discharging the system can be considered as a parallel RLC circuit consisting of the inductor L, the load $R_{\rm load}$ and a parasitic capacitance C that is connected between the load and gnd. A conservative value of $C = 5$ pF was chosen as an upper limit for the capacitance due to the bondpads, ESD protection, package pins and other parasitic effects.

Conventional dynamic supplies use an output capacitor $C_{\rm out} \gg C$, which will usually cause the parallel RLC circuit to be underdamped. Without $C_{\rm out}$ this 2nd order circuit is likely to be overdamped (which holds for $\zeta = \sqrt{T/(2RC)}H > 1$). The response of the system is: $V_{\rm out} = A\exp(s_1t) + B\exp(s_2t)$. The real valued time constants $-s_1^{-1}$ and $-s_2^{-1}$ determine how fast the response decays. Taking the largest time constant $\tau = \max(-s_1^{-1}, -s_2^{-1})$, it was chosen to have $(1-\delta_{\rm max}) > 2\tau$. Calculating τ in terms of L gives

$$L < -\frac{RT^2(\delta_{\rm max} - 1)^2}{2(T\delta_{\rm max} - T + 2RC)}. \tag{4}$$

Equations (3) and (4) are plotted in Fig. 7 for maximum and minimum load conditions. Based on this figure it was chosen to have $L = 22$ μH for which $0.105 < H < 0.33$ over the full range of $R_{\rm load}$.

2) Conduction and Switching Losses: The sizing of transistors M_1–M_5 is important to find a trade-off between the conduction and switching losses. To analyze the response of the system including both conduction and switching losses, the circuit as depicted in Fig. 8 is analyzed, which includes the most dominant parasitic elements. During the charging phase S_2 and S_4

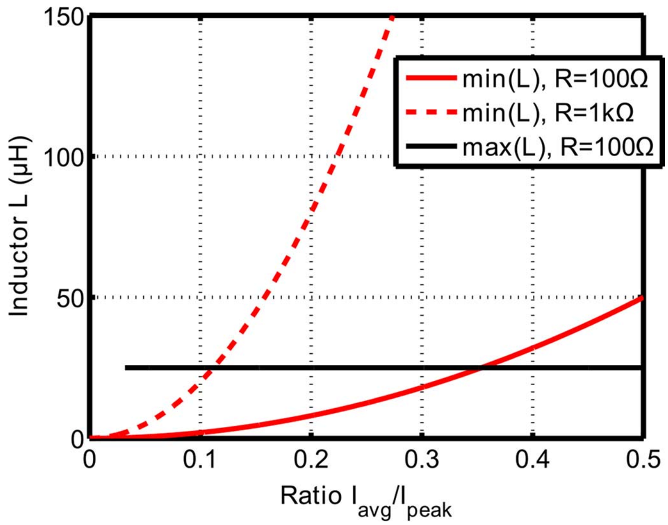

Fig. 7. Maximum and minimum values of L for different load conditions as a function of $H = I_{\mathrm{avg}}/I_{\mathrm{peak}}$.

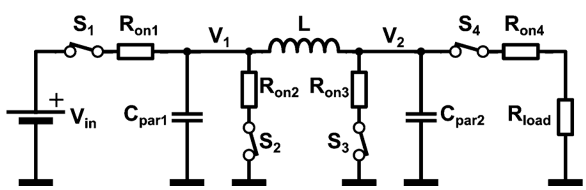

Fig. 8. Forward buck-boost converter circuit including conduction (R_{on}) and switching (C_{par}) losses.

are opened and can be removed from the circuit. Using Kirchhoff's Current Law (KCL) the following equations are obtained:

$$\frac{v_1 - V_{dd}}{R_{\mathrm{on1}}} + C_{\mathrm{par1}}\frac{dv_1}{dt} + \frac{1}{L}\int (v_1 - v_2)dt = 0 \tag{5a}$$

$$\frac{v_2}{R_{\mathrm{on2}}} + C_{\mathrm{par2}}\frac{dv_2}{dt} + \frac{1}{L}\int (v_2 - v_1)dt = 0. \tag{5b}$$

By substituting (5b) into (5a) the following third order differential equation can be found:

$$\begin{aligned} &LC_{\mathrm{par1}}C_{\mathrm{par2}}\frac{d^3v_2}{dt^3} + \left[\frac{LC_{\mathrm{par2}}}{R_{\mathrm{on1}}} + \frac{LC_{\mathrm{par1}}}{R_{\mathrm{on2}}}\right]\frac{d^2v_2}{dt^2} \\ &+ \left[\frac{L}{R_{\mathrm{on1}}R_{\mathrm{on2}}} + C_{\mathrm{par1}} + C_{\mathrm{par2}}\right]\frac{dv_2}{dt} \\ &+ \left[\frac{1}{R_{\mathrm{on1}}} + \frac{1}{R_{\mathrm{on2}}}\right]v_2 = \frac{V_{dd}}{R_{\mathrm{on1}}}. \end{aligned} \tag{6}$$

The roots s_1, s_2 and s_3 of the characteristic cubic equation can be found and by subsequently solving the particular solution, the following form for $v_2(t)$ is obtained:

$$\begin{aligned} v_2(t) = \mathrm{Re}\Big\{&K_1\exp(s_1 t) + K_2\exp(s_2 t) \\ &+ K_3\exp(s_3 t) + \frac{V_{dd}R_{\mathrm{on2}}}{R_{\mathrm{on1}} + R_{\mathrm{on2}}}\Big\}. \end{aligned} \tag{7}$$

Here K_1, K_2 and K_3 are found by solving the equations for the the initial conditions $v_2(0) = 0$ V, $(dv_2(0))/(dt) = 0$ and $(dv_2^2(0))/(dt^2) = 0$, meaning that it is assumed that at the beginning of a new stimulation cycle there is no energy left in the dynamic components

$$K_1 = \frac{-Zs_2s_3}{(s_1 - s_2)(s_1 - s_3)} \tag{8a}$$

$$K_2 = \frac{Zs_1s_3}{(s_1 - s_2)(s_2 - s_3)} \tag{8b}$$

$$K_3 = \frac{-Zs_1s_2}{s_1s_2 - s_1s_3 - s_2s_3 + s_3^2}. \tag{8c}$$

Here $Z = (V_{dd}R_{\mathrm{on2}})/(R_{\mathrm{on1}} + R_{\mathrm{on2}})$. A very similar approach can be used to solve the circuit during the discharge phase. Now S_1 and S_3 are opened and can be removed from the circuit. Again by using the KCL and by using substitution, the following differential equation can be found:

$$\begin{aligned} &LC_{\mathrm{par1}}C_{\mathrm{par2}}\frac{d^3v_2}{dt^3} + \left[\frac{LC_{\mathrm{par2}}}{R_{\mathrm{on3}}} + \frac{LC_{\mathrm{par1}}}{(R + R_{\mathrm{on4}})}\right]\frac{d^2v_2}{dt^2} \\ &+ \left[\frac{L}{R_{\mathrm{on3}}(R + R_{\mathrm{on4}})} + C_{\mathrm{par1}} + C_{\mathrm{par2}}\right]\frac{dv_2}{dt} \\ &+ \left[\frac{1}{R_{\mathrm{on3}}} + \frac{1}{R + R_{\mathrm{on4}}}\right]v_2 = 0. \end{aligned} \tag{9}$$

Solving again for the roots s_1, s_2 and s_3 of this equation leads to the following expression:

$$v_2(t) = \mathrm{Re}\left\{K_1\exp(s_1 t) + K_2\exp(s_2 t) + K_3\exp(s_3 t)\right\} \tag{10a}$$

$$K_1 = \frac{Z - Ys_2 - Ys_3 + Xs_2s_3)}{(s_1 - s_2)(s_1 - s_3)} \tag{10b}$$

$$K_2 = \frac{-(Z - Ys_1 - Ys_3 + Xs_1s_3)}{(s_1 - s_2)(s_2 - s_3)} \tag{10c}$$

$$K_3 = \frac{Z - Ys_1 - Y_s2 + Xs_1s_2}{s_1s_2 - s_1s_3 - s_2s_3 + s_3^2}. \tag{10d}$$

Here $X = v_2(0)$, $Y = (dv_2(0))/(dt) = C_{\mathrm{par2}}^{-1}(I_L(0) - (V_2(0))/(\mathrm{Ron4} + R))$ and $Z = (dv_2^2(0))/(dt^2) = (\mathrm{LC}_{\mathrm{par2}})^{-1}(V_1(0) - V_2(0) - (\mathrm{LY})/(\mathrm{Ron4} + R))$ are constants determined by the initial conditions $v_1(0)$, $I_L(0)$ and $v_2(0)$ that are set by the corresponding values at the end of the charging phase. Using the expressions for $v_2(t)$, the expressions for $I_L(t)$ and $v_1(t)$ follow from the circuit.

The energy delivered by the source during the charging phase equals: $E_s = \int V_{\mathrm{in}}(V_{\mathrm{in}} - v_1(t))/R_{\mathrm{on1}}dt$. The energy dissipated in the source during the discharge phase is found as $E_l = \int v_2^2(t)R/(R+R_{\mathrm{on4}})^2dt$. The total power efficiency is now calculated as $\eta_{\mathrm{total}} = E_l/E_s$.

The values of R_{on} and C_{par} can be found based on the parasitic components of the specific transistors as a function of their size. The bondpads, ESD circuitry and package pins are again assumed to add an additional 5 pF to C_{par}. By iteratively evaluating the equations for various transistor sizes, a trade-off is found between conduction and switching losses. The calculated

This article has been accepted for inclusion in a future issue of this journal. Content is final as presented, with the exception of pagination.

TABLE II
TRANSISTOR SIZES FOR THE CIRCUIT IN FIG. 6

Transistor	Size (W/L)
M_1	4800 μm/600 nm
M_2	1440 μm/200 nm
M_3	1680 μm/200 nm
M_4	1000 μm/600 nm
M_5	640 μm/200 nm

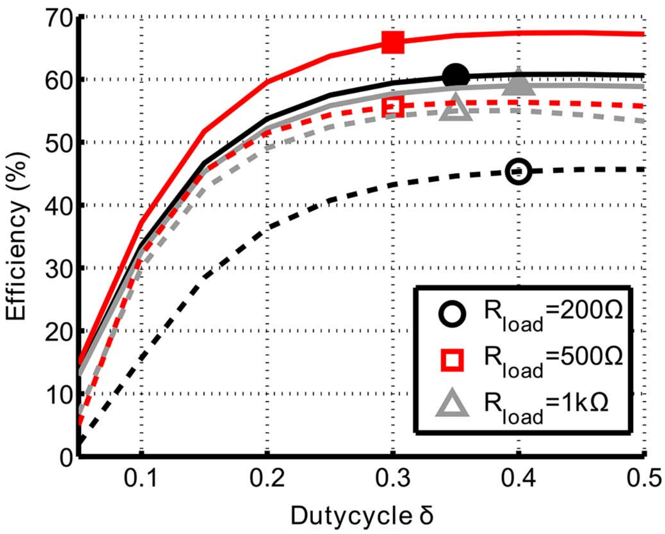

Fig. 9. Calculated (solid lines, filled markers) and simulated (dashed lines, open markers) power efficiency of the dynamic stimulator circuit. Simulations include losses due to conduction, switching, gate drivers, bondpads and non-ideal inductor.

efficiency for various loads as a function of the duty cycle for the chosen transistor dimensions (see Table II) is shown in Fig. 9.

Using the obtained transistor sizes, the circuit from Fig. 6 is simulated including gate driver and level converter circuitry. An inductor model that includes losses based on realistic inductors (Epcos 22 μH inductor with series resistance $R_s = 70$ mΩ and parallel capacitance $C_p = 3.75$ pF) is included. The simulation results are depicted in Fig. 9 as well. The efficiency is degraded with respect to the calculations due to three effects. First the implementation of the various components such as the drivers and the inductor introduces power losses. Second the voltage drop over diode D_1 was not accounted for in the previous calculations. Third, V_{gs} of transistor M_4 depends on the output voltage, because the gate is connected to gnd (it is not bootstrapped). For low output voltages (corresponding to low R_{load} and/or low δ), the second and third effect become dominant.

B. Clock and Duty Cycle Generator

The clock signals *CLK_LF*, *CLK_HF* and *DUTY* are all generated using the relaxation oscillator that is depicted in Fig. 10. The circuit uses a threshold compensated inverter [25] to implement a Schmitt trigger as was introduced in [26].

The bias current I_{bias} is used to charge capacitor C_1 by enabling the right hand side transmission gate using SW_1. Once V_{cap} reaches the first threshold of the Schmitt trigger, SW_1 is opened and SW_2 closes, which causes the current direction through C_1 to reverse via current mirror M_1-M_2. This causes

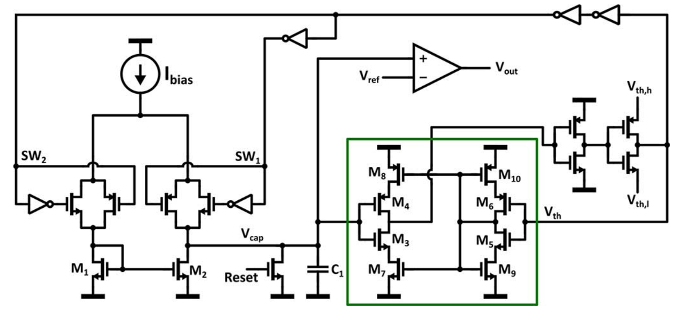

Fig. 10. Relaxation oscillator circuit used to generate the (duty cycled) clock signals. The circuit uses a Schmitt trigger that is implemented using a threshold compensated inverter, which is highlighted in the green box. The comparator is used to generate the *CLK_HF* and *DUTY* signals.

the voltage of C_1 to decrease again, until the second threshold of the Schmitt trigger is reached, which cause SW_1 and SW_2 to return to their original state, completing a clock period.

The threshold compensated inverter is highlighted in the box in Fig. 10. M_3 and M_4 form the inverter for which the threshold voltage is set by biasing M_7 and M_8 using the V_{th} signal. M_5 and M_6 are copies of M_3 and M_4 and generate the required biasing via the feedback loop comprising M_9 and M_{10}. The two thresholds of the Schmitt trigger are realized by switching V_{th} between $V_{th,l}$ and $V_{th,h}$ as shown in the figure.

The static current consumption through the branch M_{10}-M_6 -M_5-M_9 is minimized by two mechanisms [26]. First of all V_{th} is chosen to be close to either V_{dd} or gnd, which switches off M_9 or M_{10} respectively and which leads to a large amplitude for V_{cap}. Second of all the length of M_9 and M_{10} can be increased, while the resulting V_{th} due to mismatch with M_7 and M_8 is very small.

The *CLK_LF* generator uses the SW_1 signal to obtain the output signal *CLK_LF*. The bias current for this block is 10 nA and the average simulated power consumption (including the $V_{th,l}$ and $V_{th,h}$ references) is 1.33 μW.

The 1 MHz duty cycled generator uses the triangular waveform of V_{cap} to generate a duty cycled signal by using the comparator as shown in Fig. 10. The value of V_{ref} is set using a Digital to Analog Converter (DAC) using a standard R-2R structure ($R \approx 15$ kΩ) that is depicted in Fig. 11. As can be seen the *CLK_HF* signal is also derived from V_{cap} in order to make sure that *DUTY* is aligned with *CLK_HF*.

The average power consumption of the whole duty cycle generator over the full range of the DAC is simulated to be 176.2 μ W. Notice that this block will only be active during stimulation and hence the average power consumption in a real situation will be much lower.

V. EXPERIMENTAL RESULTS

The complete system has been implemented in 0.18 μ m AMS H18 High Voltage technology. The digital control system is realized by synthesizing the Verilog description and occupies 0.25 mm^2. The total chip area of 3.36 mm^2 is pad limited and the microphotograph of the IC with the various functional blocks highlighted is depicted in Fig. 12.

Besides V_{in} the system needs two more supply voltages. The supply voltage of the digital core as well as the clock generator

This article has been accepted for inclusion in a future issue of this journal. Content is final as presented, with the exception of pagination.

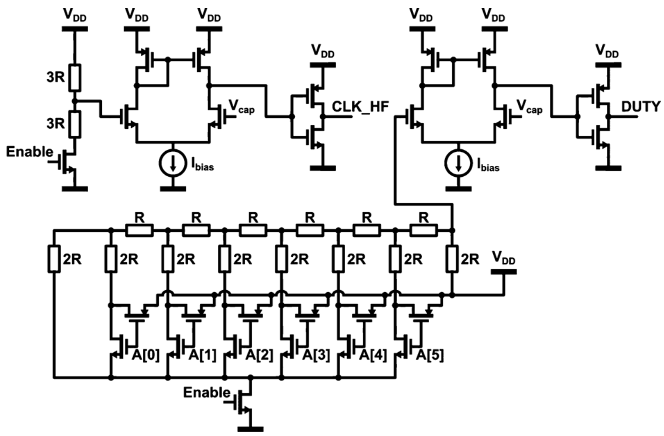

Fig. 11. DAC and comparator design used to generate the CLK_HF and DUTY outputs of the high frequency generator. The signal $V_{\rm cap}$ is connected to the same signal from Fig. 10.

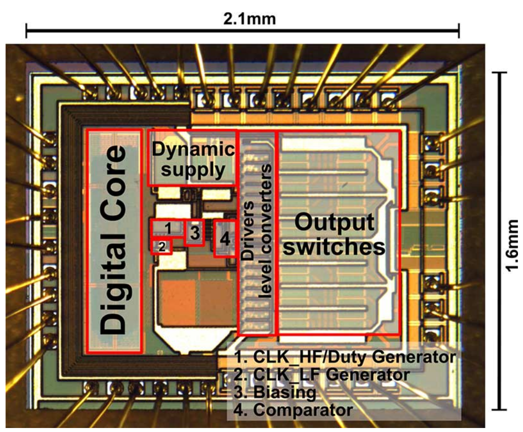

Fig. 12. Microphotograph of the IC with the functional blocks highlighted.

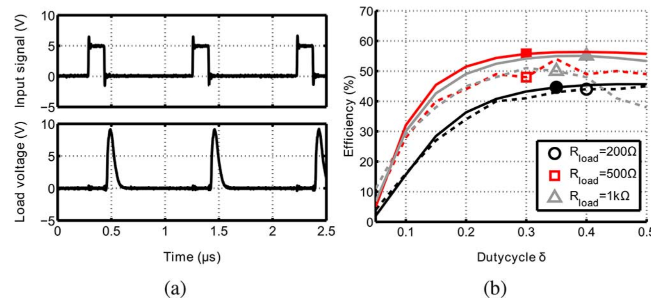

Fig. 13. In (a) the transient operation of the system during a power efficiency measurement is shown. The settings used for this measurement were $V_{\rm in} = 3.5$ V, $\delta = 0.15$, $R_{\rm load} = 1$ kΩ. In (b) the power efficiency of the dynamic stimulator is plotted for various loads and duty-cycles. Solid lines (filled markers) are the measurement results, while the dashed lines (open markers) are the simulation results.

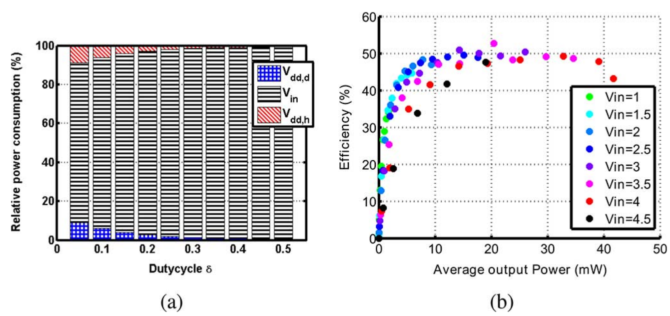

Fig. 14. In (a), a breakdown of the power consumption of each power supply is given as a function of δ ($R_{\rm load} = 500\ \Omega$). The power consumption from the digital control block is excluded. In (b), the power efficiency for a 500 Ω load is depicted for various values of $V_{\rm in}$.

blocks is $V_{dd,d} = 1.8$ V. The drivers of M_4 from Fig. 6 need $V_{dd,h} = 20$ V. The inductor used for the buck-boost system is the EPCOS B82464G4223M.

A. Power Efficiency

The power efficiency of the buck-boost converter system is determined for various loads and stimulation intensities. The system is first configured to stimulate a resistive load continuously in one direction. In Fig. 13(a) an example is given of the waveform that is measured in this configuration.

Using a Keithley 6430 sourcemeter the average power supplied by the voltage sources is measured. The transient voltage $V_{\rm out}$ over the load is captured using a Tektronix TDS2014C oscilloscope and the average power is determined by calculating $T^{-1}\int V_{\rm out}^2/R_{\rm load}dt$ using Matlab.

The measured power efficiency of the dynamic converter (including the losses in the gate drivers and the current from $V_{dd,h}$) is depicted in Fig. 14. As can be seen the measurements are in close correspondence with the simulation results. For high δ and high $R_{\rm load}$, the efficiency goes down, because the output voltage is clipping to the supply voltage $V_{dd,h}$. In Fig. 14(a) a breakdown of the power consumption is given as a function of the duty cycle ($R_{\rm load} = 500\ \Omega$).

In Fig. 14(b) the power efficiency of the dynamic stimulator is measured for varying $V_{\rm in}$ in case of $R_{\rm load} = 500\ \Omega$. As can be seen, the power efficiency of the system continues to be relatively high, although the available output power decreases for lower $V_{\rm in}$.

B. Bihphasic Stimulation Pulse

First a single channel is configured for a biphasic stimulation waveform with $\delta = 0.17$. The pulse width is 200 μ s and the pattern repetition rate is 3.92 Hz. The load is modeled using $R_{\rm load} = 560\ \Omega$ and $C_{dl} = 1\ \mu$F.

The resulting waveform is depicted in Fig. 15(a). The biphasic stimulation waveform has the expected shape and in Fig. 15(b) a detail of the stimulation waveform is given at the beginning of the first stimulation phase. After the biphasic stimulation pulse is finished, pulse insertion is used to remove the remaining charge from C_{dl}.

C. Multichannel Operation

In Fig. 16(a) multichannel operation is demonstrated by activating four channels simultaneously. During the first 500 μs the SPI interface loads the stimulation settings for each channel individually and subsequently a single 'trigger global' command is given. Channel 1 starts immediately $(\rm sync = 0)$, channel 2 and 3 start 1 ms later $(\rm sync = 1)$, while channel 4 starts 2 ms later $(\rm sync = 2)$.

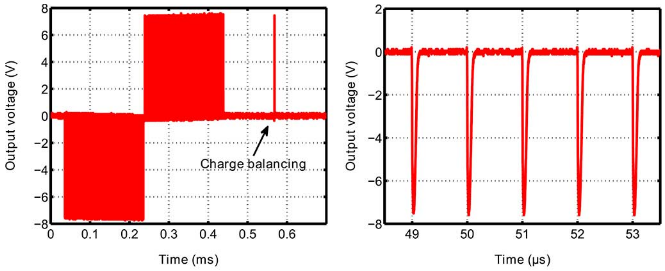

(a) (b)

Fig. 15. Measured biphasic stimulation waveform using $t_{\mathrm{stim}} = 200\ \mu$s and $\delta = 0.17$ over a load of $R_{\mathrm{load}} = 560\ \Omega$ and $C_{dl} = 1\ \mu$F.

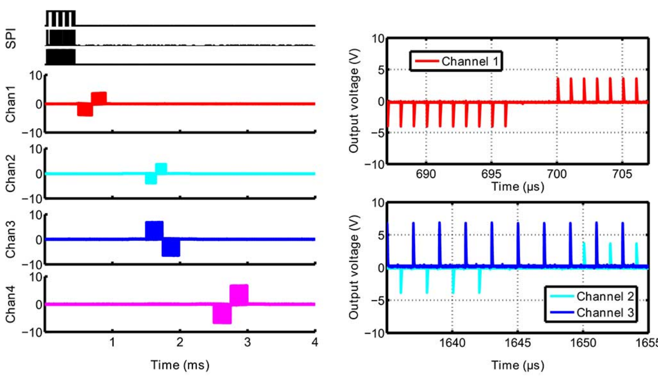

(a) (b)

Fig. 16. Measurement results showing the multichannel operation of the system. In (a), the programming phase using SPI is shown for $t < 0.5$ ms, while afterwards 4 independent channels are shown. In (b), a detail is given for channel 1 and channel 2/3.

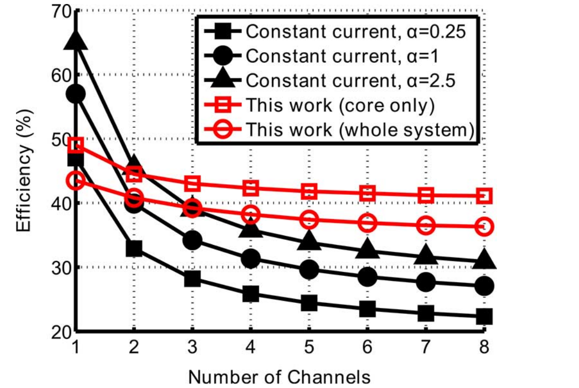

Fig. 17. Measurement results showing the power efficiency of the multichannel operation of the system (red lines). These results are compared with the calculated inefficiencies of a classical constant current system with adaptive supply (black lines).

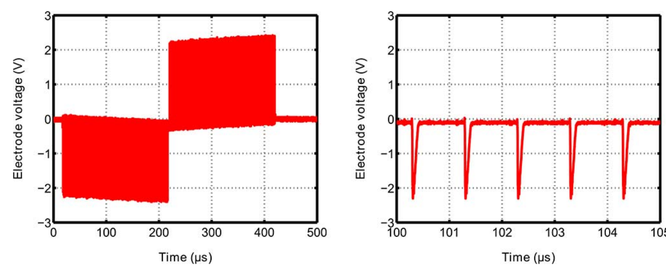

(a) (b)

Fig. 18. Measured stimulation waveform for DBS electrodes submerged in a PBS solution bath.

The detailed plots in Fig. 16(b) show that the simultaneous multichannel operation is working as expected: when two channels are active simultaneously, the pulses are alternately injected in each channel. Moreover it is seen that two channels can be stimulated simultaneously with opposite polarity, different pulsewidths and amplitudes.

The power efficiency of the system in multichannel mode is compared to a constant current source with adaptive supply voltage. The first channel of the system is configured with a biphasic stimulation pulse with $\delta = 0.4$ through a load of $R_{\mathrm{load}} = 500\ \Omega$. According to the measured average power in the load, this corresponds to an average $I_{\mathrm{stim}} = 6.9$ mA. Additional channels are connected with $R_{\mathrm{load}} = 200\ \Omega$. For each channel the same average I_{stim} is used, which corresponds to $\delta = 0.15$. The power efficiency of the proposed system in this configuration is shown in Fig. 17.

The equations from Section II.A with $\eta_{\mathrm{supply}} = 80\%$ and $V_{\mathrm{compl}} = 300$ mV are used to determine the power efficiency of a realistic adaptive supply constant current stimulator in this situation for various values of α. As can be seen from Fig. 17, the system proposed in this work outperforms the adaptive power supply stimulator when operated using 2 or more channels. For low values of α this improvement can be as large as 200%.

D. PBS Solution Measurements

The response of the system connected to electrodes in a Phosphate Buffered Saline (PBS) solution is measured. The platinum ring shaped electrodes with area 14 mm^2 as discussed earlier are submerged in a PBS solution bath. For the stimulation settings it was chosen to have $\delta = 0.15$ and $t_{\mathrm{stim}} = 200\ \mu$s. The resulting electrode voltage is shown in Fig. 18 and looks very similar to the result from the series RC model.

E. Discussion

In Table III the performance of the prototype is summarized and compared to other recent stimulator designs. As compared to other systems, this work offers more flexibility in the electrode configuration, which is important for current steering applications. Furthermore, the efficiency for single channel operation is slightly lower than the other systems, but this is compensated when the system is operated in multichannel mode: in this case the efficiency remains almost constant (see Fig. 17). The efficiency listed in this table refers to the stimulator output stage only and does not include other system components such as an inductive link and rectifier.

The power efficiency of the system can be further improved, especially by reducing the losses in D_1 and M_4 from the circuit in Fig. 6. These devices could be combined in a single transistor that is operated with bootstrapping, which will significantly reduce the losses for low output voltages. Moreover, the power efficiency of the duty-cycle generator can be improved by designing a more power efficient DAC topology.

The system currently still needs two external supplies: one low supply for the digital control and one high supply for the HV switches. Future implementations can integrate the required

TABLE III
COMPARISON OF PERFORMANCE

	[17]	[3]	[13]	[11]	This work
Type	Filtered dyn. supply	Current Source	Current Source	Current Source	Unfiltered dyn. supply
Application	General Purpose	Retinal	DBS	Proprioceptive	General purpose
Channels	1	256 (2)*	1	1	8
Electrodes	2	1024 (8)*, monopolar	4 (Bipolar)	8 (Bipolar)	16 (fully arbitrary)
Power Source	Battery (3.3V)	Inductive Link	Inductive Link	Battery	Battery
HV Generation	N.A.	Rectifier (±10V)	Adaptive rectifier (4.6V)	Integrated charge pump	External (20V)
Process	0.35μ	0.35μ	0.5μ	0.18μ	0.18μ
I_{stim}	N.A.	$4-992\,\mu$A	$80-2\,480\,\mu$A	$2-504\,\mu$A	$<10\,$mA
Load impedance	$500-2\,000\,\Omega$	$<10\,$kΩ	$2\,$kΩ	7kΩ	$100-1\,000\,\Omega$
Stimulator Efficiency	35-50%	N.A.	58-68%**	N.A.	40%
Multichannel efficiency	No	No	No	No	Yes

* Number realized in prototype is depicted in parenthesis
** Efficiency of current source only. Adaptive supply generator efficiency (72-82%) is not included

voltage converters. The power needed from $V_{dd,h}$ heavily depends on the stimulation settings, but is generally relatively low, which makes it possible to integrate a charge pump for this purpose.

The number of electrodes connected to the system in its current form cannot be increased without penalties. Each additional electrode requires an additional switch M_4 in Fig. 6, which increases the parasitic capacitance at this node, increasing the switching losses in the circuit. One possible way to overcome this is to design more sophisticated switch array configurations that aim to minimize the capacitive load.

Another limitation of the designed prototype is that it currently is operated in open loop: there is no control over the amount of injected charge, other than by controlling the duty-cycle. Future implementations can benefit from including a feedback mechanism that controls the charge delivered to the load and can compensate for variations in for example $V_{\rm in}$ and L.

One advantage of the proposed system that has not been addressed yet is that there is no driver transistor that connects V_{dd} directly to the electrodes. Such a driver transistor is found in current source based implementations and introduces a single fault failure mode for the device: when this device is shorted, a large current will flow through the electrodes. In the proposed system $V_{\rm in}$ connects to the electrode via multiple switches and hence this does not introduce a potential single fault failure mode.

It is likely that the proposed stimulation strategy can also be used for other kind of excitable tissue, such as muscle tissue. However, there is more research needed towards the effect of the high frequency current pulses on the tissue. In [19] the efficacy of this type of stimulation was shown, but little is known about the losses in the tissue and (long term) safety aspects. On the other hand it is interesting to see that the proposed stimulation principle mimics the natural working principle of neurons: the synaptic receptors continuously receive pulsating inputs that are integrated on the membrane surface of the dendritic tree. The pulsed stimulation has a similar peaking waveform.

VI. Conclusion

This paper has presented the realization of a neural stimulator system that uses an unfiltered dynamic supply to directly stimulate the target tissue. It is possible to operate the system with multiple independent channels that connect to an arbitrary electrode configuration, making the system well suited for current steering techniques. Furthermore, comprehensive control was implemented using a dual clock configuration that allows both autonomic tonic stimulation, as well as single shot stimulation. Each channel can be configured individually with tailored stimulation parameters and multiple channels can operate in a synchronized fashion.

The system is shown to be power efficient, especially when compared with state-of-the-art constant current stimulators with an adaptive power supply that operate in multichannel mode. Efficiency improvements up to 200% have been demonstrated.

Acknowledgment

The authors would like to thank the members of the Sins consortium (http://www.braininnovations.nl) for the excellent cooperation. Also, the authors would like to thank J. van Breda for the assistance during the patent filing.

References

[1] B. Bonham and L. Litvak, “Current focusing and steering: Modeling, physiology and psychophysics,” *Hear. Res.*, vol. 242, no. 1–2, pp. 141–153, Aug. 2008.
[2] D. Jiang, D. Cirmirakis, and A. Demosthenous, “A vestibular prosthesis with highly-isolated parallel multichannel stimulation,” *IEEE Trans. Biomed. Circuits Syst.*, 2014, IEEE Xplore Early Access Article, DOI: 10.1109/TBCAS.2014.2323310.
[3] E. Noorsal, K. Sooksood, H. Xu, R. Hornig, J. Becker, and M. Ortmanns, “A neural stimulator frontend with high-voltage compliance and programmable pulse shape for epiretinal implants,” *IEEE J. Solid-State Circuits*, vol. 47, no. 1, pp. 244–256, Jan. 2012.
[4] Y. Lo, K. Chen, and W. Liu, “A fully-integrated high-compliance voltage SoC for epi-retinal and neural prostheses,” *IEEE Trans. Biomed. Circuits Syst.*, vol. 7, no. 6, pp. 761–772, Dec. 2013.
[5] K. Chen, Z. Yang, L. Hoang, J. Weiland, M. Humayun, and W. Liu, “An integrated 256-channel epiretinal prosthesis,” *IEEE J. Solid-State Circuits*, vol. 45, no. 9, pp. 1946–1956, Sep. 2010.
[6] C. Butson and C. McIntyre, “Current steering to control the volume of tissue activated during deep brain stimulation,” *Brain Stim.*, vol. 1, no. 1, pp. 7–15, Jan. 2008.
[7] C. Veraart, W. Grill, and T. Mortimer, “Selective control of muscle activation with a multipolar nerve cuff electrode,” *IEEE Trans. Biomed. Eng.*, vol. 40, no. 7, pp. 640–653, July 1993.
[8] H. Martens, E. Toader, M. Decr, D. Anderson, R. Vetter, D. Kipke, K. Baker, M. Johnson, and J. Vitek, “Spatial steering of deep brain stimulation volumes using a novel lead design,” *Clin. Neurophys.*, vol. 122, no. 3, pp. 558–566, Mar. 2011.
[9] V. Valente, A. Demosthenous, and R. Bayford, “A tripolar current-steering stimulator ASIC for field shaping in deep brain stimulation,” *IEEE Trans. Biomed Circuits Syst.*, vol. 6, no. 3, pp. 197–207, Jun. 2012.

[10] K. Sooksood, E. Noorsal, U. Bihr, and M. Ortmanns, "Recent advances in power efficient output stage for high density implantable stimulators," in *Proc. IEEE Annu. Int. Conf. Engineering in Medicine and Biology Soc.*, Sep. 2012, pp. 855–858.

[11] I. Williams and T. Constandinou, "An energy-efficient, dynamic voltage scaling neural stimulator for a proprioceptive prosthesis," *IEEE Trans. Biomed. Circuits Syst.*, vol. 7, no. 2, pp. 129–139, Apr. 2013.

[12] C. Lin, W. Chen, and M. Ker, "Implantable stimulator for epileptic seizure suppression with loading impedance adaptability," *IEEE Trans. Biomed. Circuits Syst.*, vol. 7, no. 2, pp. 196–203, Apr. 2013.

[13] H.-M. Lee, H. Park, and M. Ghovanloo, "A power-efficient wireless system with adaptive supply control for deep brain stimulation," *IEEE J. Solid-State Circuits*, vol. 48, no. 9, pp. 2203–2216, Sep. 2012.

[14] J. Randles, "Kinetics of rapid electrode reactions," *Discuss. Faraday Soc.*, vol. 1, pp. 11–19, 1947.

[15] C. Butson, C. Maks, and C. McIntyre, "Sources and effects of electrode impedance during deep brain stimulation," *Clin. Neurophys.*, vol. 117, no. 2, pp. 447–454, Feb. 2006.

[16] T. Cheung, M. Nu, M. Hoffman, M. Katz, C. Kilbane, R. Alterman, and M. Tagliati, "Longitudinal impedance variability in patients with chronically implanted dbs devices," *Brain Stim.*, vol. 6, pp. 746–751, 2013.

[17] S. Arfin and R. Sarpeshkar, "An energy-efficient, adiabatic electrode stimulator with inductive energy recycling and feedback current regulation," *IEEE Trans. Biomed. Circuits Syst.*, vol. 6, no. 1, pp. 1–14, Feb. 2012.

[18] M. van Dongen and W. Serdijn, "A switched-mode multichannel neural stimulator with a minimum number of external components," in *Proc. IEEE Int. Symp. Circuits and Systems*, May 2013, pp. 1877–1880.

[19] M. van Dongen, F. Hoebeek, S. Koekkoek, C. de Zeeuw, and W. Serdijn, Efficacy of High Frequency Switched-Mode Stimulation in Activating Purkinje Cells, Jun. 2014 [Online]. Available: http://arxiv.org/abs/1406.7185

[20] E. Warman, W. Grill, and D. Durand, "Modeling the effects of electric fields on nerve fibers: Determination of excitation thresholds," *IEEE Trans. Biomed. Eng.*, vol. 39, no. 12, pp. 1244–1254, Dec. 1992.

[21] J. Malmivuo and R. Plonsey*, Bioelectromagnetism—Principles and Applications of Bioelectric and Biomagnetic Fields*. New York, NY, USA: Oxford Univ. Press, 1995.

[22] A. Kuncel and W. Grill, "Selection of stimulusd parameters for deep brain stimulation," *Clin. Neurophys.*, vol. 115, no. 11, pp. 2431–2441, Nov. 2004.

[23] K. Slavin, "Peripheral nerve stimulation for neuropathic pain," *Neurotherapeutics*, vol. 5, pp. 100–106, Jan. 2008.

[24] K. Sooksood, T. Stieglitz, and M. Ortmanns, "An active approach for charge balancing in functional electrical stimulation," *IEEE Trans. Biomed. Circuits Syst.*, vol. 4, no. 3, pp. 162–170, Jun. 2010.

[25] M.-T. Tan, J. Chang, and Y.-C. Tong, "A process-independent threshold voltage inverter-comparator for pulse width modulation applications," in *Proc. 6th IEEE Int. Conf. Electronics, Circuits and Systems*, 1999, vol. 3, p. 1201.

[26] M. van Dongen and W. Serdijn, "Design of a low power 100 db dynamic range integrator for an implantable neural stimulator," in *Proc. IEEE Biomedical Circuits and Systems Conf*, Nov. 2010, pp. 158–161.

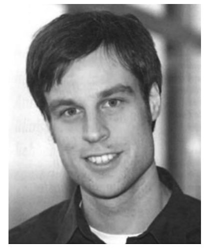

Marijn N. van Dongen (S'11–M'14) was born in Pijnacker, The Netherlands, in 1984. He received the B.Sc. (*cum laude*) and M.Sc. degrees in electrical engineering from the Delft University of Technology, Delft, The Netherlands, in 2007 and 2010, respectively.

He is working toward the Ph.D. degree in section bioelectronics in the Microelectronics Department of the Delft University of Technology. His research interests include the design of neural stimulator output circuits as well as the modeling of the electrophysiological and electrochemical processes during electrical stimulation. Currently, he is working for NXP Semiconductors, Nijmegen, The Netherlands.

Mr. van Dongen served as the Financial Chair of the IEEE BioCAS2013 Conference.

Wouter A. Serdijn (M'98–SM'08–F'11) was born in Zoetermeer (Sweet Lake City), The Netherlands, in 1966. He received the M.Sc. (*cum laude*) and Ph.D. degrees from the Delft University of Technology, Delft, The Netherlands, in 1989 and 1994, respectively.

His research interests include low-voltage, ultra-low-power and ultra wideband integrated circuits and systems for biosignal conditioning and detection, neuroprosthetics, transcutaneous wireless communication, power management and energy harvesting as applied in, e.g., hearing instruments, cardiac pacemakers, cochlear implants, portable, wearable, implantable and injectable ExG recorders and neurostimulators. He is coeditor and coauthor of the books *Ultra Low-Power Biomedical Signal Processing: An Analog Wavelet Filter Approach for Pacemakers* (New York, NY, USA: Springer, 2009), *Circuits and Systems for Future Generations of Wireless Communications* (New York, NY, USA: Springer, 2009), *Power Aware Architecting for Data Dominated Applications* (New York, NY, USA: Springer, 2007), *Adaptive Low-Power Circuits for Wireless Communications* (New York, NY, USA: Springer, 2006), *Research Perspectives on Dynamic Translinear and Log-Domain Circuits* (Norwell, MA, USA: Kluwer, 2000), *Dynamic Translinear and Log-Domain Circuits* (Norwell, MA, USA: Kluwer, 1998), and *Low-Voltage Low-Power Analog Integrated Circuits* (Norwell, MA, USA: Kluwer, 1995). He authored and coauthored six book chapters and more than 250 scientific publications and presentations. He teaches Circuit Theory, Analog Signal Processing, Micropower Analog IC Design and Bioelectricity. He received the Electrical Engineering Best Teacher Award in 2001 and 2004.

Dr. Serdijn has served, a.o., as Technical Program Chair for IEEE BioCAS 2010 and as Technical Program Chair for IEEE ISCAS 2010 and 2012, as a member of the Board of Governors (BoG) of the IEEE Circuits and Systems Society (2006–2011), as Chair of the Analog Signal Processing Technical Committee of the IEEE Circuits and Systems Society, as a member of the Steering Committee of the IEEE TRANSACTIONS ON BIOMEDICAL CIRCUITS AND SYSTEMS (T-BioCAS) and as Editor-in-Chief for IEEE TRANSACTIONS ON CIRCUITS AND SYSTEMS—I: REGULAR PAPERS (2010–2011). He was General Co-Chair for IEEE BioCAS 2013 and TPC Co-Chair for IEEE ISCAS 2014, and will be General Co-Chair for IEEE ISCAS 2015. He is an IEEE Distinguished Lecturer and a mentor of the IEEE.